ACS Photonics

Article

pubs.acs.org/journal/apchd5

Graphene-Based Plasmonic Platform for Reconfigurable Terahertz Nanodevices

Pai-Yen Chen,*[,†,‡] Haiyu Huang,[†] Deji Akinwande,[†] and Andrea Alù*[,†]

[†]Department of Electrical and Computer Engineering, University of Texas at Austin, Austin, Texas 78712, United States

[‡]Department of Electrical and Computer Engineering, Wayne State University, Detroit, Michigan 48202, United States

Supporting Information

ABSTRACT: We propose here a new platform to realize a plethora of graphene-based plasmonic nanodevices for frequency-agile terahertz (THz) frontend circuits. We demonstrate that a class of hybrid electronic-plasmonic nanodevices combining active graphene field-effect transistors (GFET) and graphene plasmonic waveguides (GPWG) supporting tightly confined propagation of THz signals, with tailored phase velocity and characteristic impedance controlled by the gate and drain voltages of GFET. We propose a variety of reconfigurable graphene-based nanodevices based on this general architecture, including reconfigurable and electronically programmable phase-shifters, filters, transformers, modulators, and terminators. We envision the integration of these THz circuit elements into a fully reconfigurable THz system as a fundamental step toward new design architectures and protocols for THz communication, sensing, actuation, and biomedical applications.

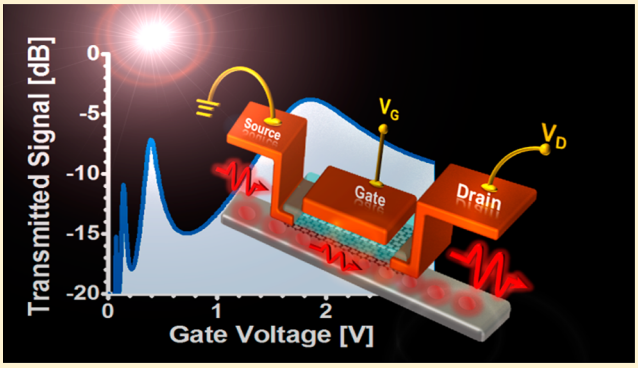

KEYWORDS: *graphene, plasmonics, terahertz, graphene devices, graphene plasmonics, graphene optoelectronics*

Graphene is an ideal gapless semiconductor (or semimetal) and truly two-dimensional (2-D) carbon nanomaterial[1,2] that has attracted large attention since its discovery in 2004.[1,2] It uniquely possesses massless, linear electron−hole dispersion and high carrier mobility and Fermi velocity $\nu_F = 10^8$ cm/s at low energies.[3] Due to its electronic structure, a broad range of charge-carrier densities can be induced in graphene by either chemical or electronic doping, allowing the shift of Fermi level over a large range.[1−4] Recently, graphene plasmonics at THz and infrared frequencies has drawn widespread attention due to its anomalous physics of tunable, collective oscillations of massless Dirac Fermions and the numerous exciting applications that it could enable.[4−24] Graphene opens many possibilities to tailor the collective excitation and propagation of surface plasmon polariton (SPP) waves in the THz and infrared spectrum.[4−24] In this frequency range, graphene's complex-valued conductivity $\sigma_s = \sigma_s' - i\sigma_s''$ [S] is tunable by varying the Fermi energy E_F (eV; see Supporting Information, Figure S1); here an $e^{-i\omega t}$ notation is adopted. Besides, high-quality graphene enables the efficient coupling of electromagnetic fields to localized surface plasmons with a significantly shortened guided wavelength. With the rapid advent of nanofabrication techniques,[16,25] graphene arguably provides an important path toward reconfigurable THz and infrared plasmonic, electronic and optoelectronic systems.[1−24] Graphene plasmonics have already found a variety of potential applications, including flat-land transformation optics,[10] invisibility cloaks,[11,12] absorbers,[13,14] broadband polarizers,[15] tunable filters and metamaterials,[16] oscillators,[8,23] modulators,[18−20] photomixers,[26−28] chip-scale THz nanopatch antennas,[29,30] and phase-shifters.[31] These become even more interesting if we consider that recent layouts of electronic and photonic devices support on-chip integrated THz wave sources, such as quantum cascade lasers (QCL),[32,33] graphene-based photomixers,[26−28] or millimeter-wave sources followed by multiple nonlinear stages of harmonic generation.[32,33]

Interestingly, when two graphene sheets are separated by a deeply subwavelength distance, a monomodal parallel-plate waveguide[31,34] is formed, supporting tightly confined, quasi-transverse-electromagnetic (quasi-TEM) modes with no cutoff frequency.[31,34] Due to the fact that the electric field is symmetric and its transverse components are negligible at the center of the waveguide,[31,34] the same mode can be supported by a graphene monolayer deposited on a dielectric coated conducting ground plane, as shown in the bottom panel of Figure 1b. This structure supports a "half-mode" waveguide[35] and is commonly used to reduce the size of planar waveguiding structures in high-frequency circuits.[35]

In this paper, we propose models and designs of vertically integrated GFET-GPWG nanodevices, as in Figure 1c, in which a monomodal GPWG is connected to the source input (S) and drain output (D), and the THz signal transmission is controlled by the gate-to-source voltage V_{GS} and gate-to-drain voltage V_{DS}.

Received: February 5, 2014
Published: July 7, 2014

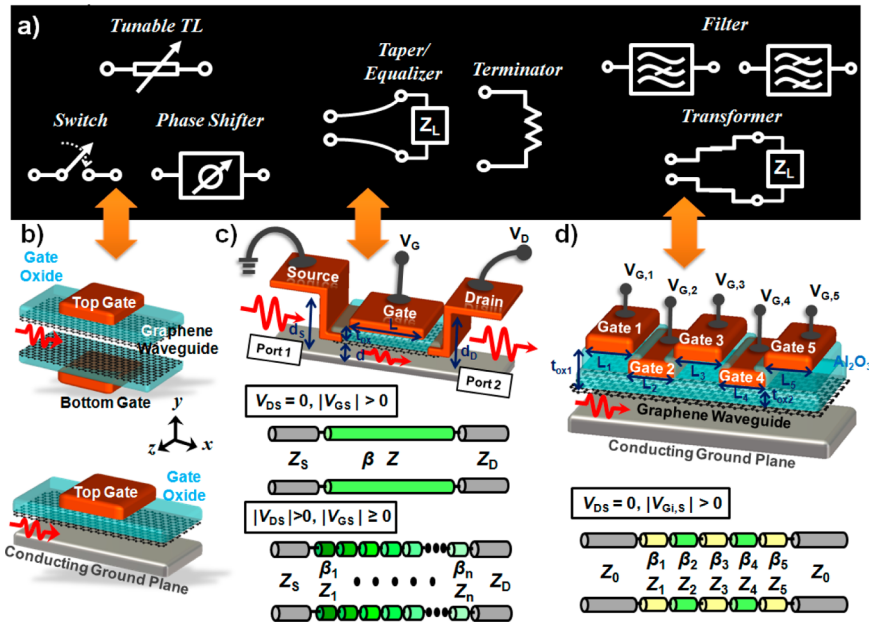

Figure 1. (a) Basic components for reconfigurable THz transceiver/receiver front-end circuit components. Their practical realization using graphene nanodevices is shown in (b–d). (b) Tunable graphene plasmonic waveguide formed by two monolayers (top panel) and a monolayer backed by a metal ground (bottom panel). (c) Top panel shows the hybrid electronic-plasmonic nanodevice, comprising of a graphene field-effect transistor (GFET) and a graphene plasmonic waveguide (GPWG). Bottom panel shows the transmission-line model (TLM) for different biasing scenarios: homogeneous and inhomogeneous transmission lines are obtained by setting $V_{DS} = 0$ and $|V_{DS}| > 0$, respectively. (d) Integrally gated graphene transmission line with digitized, spatially varying phase velocity and characteristic impedance.

This three-terminal (common-source) nanodevice may enable the modulation of phase velocity, characteristic impedance and signal integrity over a large range of values in the GPWG by electrical means. The source/drain line may be realized as conventional metallic parallel-plate waveguides or microstrip lines, with the top metal layer connected to a DC bias through proper high-frequency chokes. The source line, drain line, and the monomodal GPWG share a ground plane. The input and output signals are also quasi-TEM guided modes, and impedance matching can be achieved by adjusting the heights of the source/drain line (microwaveguide interconnects) and the gate line (GPWG). Similar matching technique for discontinuous waveguide junctions has been applied in microwave circuits.[36,37] With this nanodevice architecture, signals can be guided and modulated in ultracompact graphene channel waveguide, fully compatible with existing planar CMOS technology, and therefore, they may constitute a wafer-level, integrated front-end module for THz/infrared sensing and communication systems. Figure 1a shows various THz circuit components and their proposed realization using graphene nanodevices in Figure 1b–d, which will be discussed in the following. We also propose in the Supporting Information a realistic nanofabrication route for this hybrid electronic-plasmonic graphene nanodevice platform using semiconductor processes.

RESULTS AND DISCUSSION

Figure 1c presents the proposed hybrid graphene-based nanodevices. For the GFET design, we choose a thick amorphous (α-) or polycrystalline (poly-) silicon gate with permittivity $\varepsilon_g = 11.9\varepsilon_0$, boron nitride (BN), or silicon oxide (SiO_x) gate oxide with $\varepsilon_{ox} = 4\varepsilon_0$ and thickness $t_{ox} = 25$ nm, where ε_0 is the free-space permittivity. For the GPWG design, we choose a graphene monolayer with width w much larger than the gap d, and we assume that the waveguide is filled with aluminum oxide (Al_2O_3), with $\varepsilon_d = 9\varepsilon_0$ and thickness $d = 20$ nm. The mode supported by this waveguide has a transverse magnetic field $\mathbf{H} = \hat{z}H_z(y)\exp[i(\beta x - \omega t)]$ satisfying a dispersion equation that can be obtained by imposing the surface impedance boundary condition at the graphene interface (see Supporting Information, Figure S2):

$$\frac{\varepsilon_g}{\varepsilon_{ox}}\rho_{ox}\rho_d\sigma_s - i\omega\left(\frac{\varepsilon_{ox}\rho_d\rho_g}{\rho_{ox}} + \frac{\varepsilon_d\varepsilon_g\rho_{ox}}{\varepsilon_{ox}\tanh(\rho_d d)}\right) + \frac{\rho_d(\rho_g\sigma_s - i\omega\varepsilon_g)\tanh(\rho_d d) - i\omega\varepsilon_d\rho_g}{\tanh(\rho_{ox}t_{ox})\tanh(\rho_d d)} = 0 \quad (1)$$

where $\rho_{ox} = (\beta^2 - k_{ox}^2)^{1/2}$, $\rho_d = (\beta^2 - k_d^2)^{1/2}$, $\rho_d = (\beta^2 - k_g^2)^{1/2}$, $k_d = \omega(\mu_0\varepsilon_d)^{1/2}$, $k_{ox} = \omega(\mu_0\varepsilon_{ox})^{1/2}$, $k_g = \omega(\mu_0\varepsilon_g)^{1/2}$, and μ_0 is the free-space permeability. We can extract from this equation the complex wavenumber β. For graphene plasmonic waveguides, typically slow-wave in nature,[31,34] the fields are strongly localized between the graphene monolayer and the conducting ground plane, while evanescent fields outside the waveguide decay exponentially (see Supporting Information, Figure S2). The characteristic impedance of this monomodal graphene waveguide, defined as the ratio of voltage $V = -\int_0^d E_y dy$ to current $I = H_z$, can be expressed as $Z = E_y d/H_z = \beta d/\omega\varepsilon_d$.[31,34−38] Then, the transmission line model (TLM) and the transfer matrix method (TMM)[39,40] can be used to describe the signal transmission/reflection (or insertion/return loss of signal power) in the proposed devices (see Supporting Information). For the generalized structure in Figure 1d, for instance, the exact Fermi energy in graphene, as a function of terminal voltages V_{DS} and V_{GS}, must be appropriately evaluated in order to evaluate graphene's spatially variant conductivity and associated phase, impedance, and propagation properties of

dx.doi.org/10.1021/ph500046r | ACS Photonics 2014, 1, 647−654

THz wave in the GPWG. Our graphene's conductivity model is presented in the Supporting Information. Here we assume a temperature T = 300 K and a relaxation time τ = 1 ps, as predicted for the ballistic-transport graphene with ultrahigh carrier mobility.[41−43] To date, a carrier mobility as high as 2 × 10^5 $cm^2/(V\,s)$ has been measured in the suspended graphene,[41] ∼ 4900 $cm^2/(V\,s)$ in chemical-vapor-deposited (CVD) graphene on evaporated copper films,[42] and ∼1.78 × 10^4 $cm^2/(V\,s)$ in CVD graphene on oxidized silicon substrate.[43] Therefore, the scattering rate used here is close to experimental results. As expected, the progress in developing high-quality graphene monolayer may further improve the insertion loss, phase error, and return loss of the proposed graphene nanodevices.

The Fermi energy of graphene, which is controlled by the GFET, is related to the voltage and the graphene quantum capacitance C_q: $V_{ch}(x) = E_F(x)/q = (C_{ox}/(C_{ox} + C_q/2))(V_{GS} - V_{FB} - V(x))$,[44−47] where V_{FB} is the flat band voltage (here V_{FB} = 0 is assumed), and $C_{ox} = \varepsilon_{ox}/t_{ox}$ is the oxide capacitance. The channel voltage in graphene can be modeled by the gradual channel approximation as $V(x) = (x/L)V_{DS}$.[44−47] For a relatively thick gate oxide with $C_q \gg C_{ox}$, $E_F(x) = \hbar v_F(\pi C_{ox}(V_{GS} - (x/L)V_{DS})/q)^{1/2}$ is obtained (see Supporting Information for the detailed evaluation of E_F). The proposed device has two operation schemes: (1) when both source and drain terminals are unbiased (V_{DS} = 0), the uniform and spatially invariant propagation constant β and impedance Z of GPWG can be tuned by V_{GS}, forming a tunable and homogeneous THz transmission line; (2) when the drain terminal is biased ($|V_{DS}| > 0$), the value of E_F varies along the graphene sheet,[48] showing tapered, spatially variant $\beta(x)$ and $Z(x)$ in the GPWG. The electron density variation in the graphene channel has been recently mapped experimentally for favorable bias conditions via scanning thermal microscopy (SThM) measurements, confirming the above assumptions.[48] If $|V_{DS}| > 0$, a spatially inhomogeneous carrier concentration was measured, resulting in a nonuniform local conductivity.[48] The corresponding TLMs for these two operations are illustrated in Figure 1c.

We first focus our discussion on the case in which the proposed graphene nanodevice is biased with V_{DS} = 0 and $V_{GS} > 0$. Figure 2a and b, respectively, show the contours of the magnitude of the transmission coefficient S_{21} and reflection coefficient S_{11}, varying the operating frequency and V_{GS}. The results are calculated using the TLM-TMM combined with the GFET's device model. Here we chose the gate (waveguide) length L = 380 nm, the height of waveguide at the source and drain ends $d_S = d_D = 4d$, and the impedance of source and drain lines as $Z_S = \eta_d d_S = 4\eta_d d$ and $Z_D = \eta_d d_D = 4\eta_d d$, where $\eta_d = (\mu_0/\varepsilon_d)^{1/2}$ is the intrinsic impedance of the filling material in the source, drain, and gate lines. It is seen that at certain frequencies the transmission (S_{21}) can vary from low (i.e., unbiased) to high (i.e., high V_{GS}), with complementary reflection (S_{11}), presenting distinct ON and OFF states, as highlighted in Figure 2a,b. Figure 2c and d, respectively, show the magnitude spectra of S_{21} and S_{11} for this THz switching device with V_{GS} = 1 V (onset) and V_{GS} = 0.12 V (offset). The maximum transmission (onset) is obtained when the signal is constructively phased in the gate line ($\theta = \beta[V_{GS}]L = m\pi$, m is an integer), while the minimum transmission (offset) is obtained when the signal is destructively interfered. Based on the GFET physical model, when a large gate voltage is applied, the Fermi level of graphene is shifted up, resulting in reduced β and, correspondingly, smaller phase shifts in the gated line (see Supporting Information, Figure S4). For instance, when V_{GS} = 1 V, the induced Fermi energy of 0.57 eV leads to $\beta|_{V_{GS}=1V}$ = (8.17 + i0.14) × 10^6 [rad/m] and $Z|_{V_{GS}=1V} = (26 + i\,0.43)\eta_d d$. On the other hand, when V_{GS} = 0.12 V, with a lower Fermi energy of 0.11 eV, larger values of complex phase constant and impedance are obtained as $\beta|_{V_{GS}=0.12V}$ = (19.98 + i0.34) × 10^6 and $Z|_{V_{GS}=0.12V} = (63.58 + i1.1)\eta_d d$. We note that $|S_{21}|$ shows a larger than 15 dB contrast between ON and OFF states at the operating frequency f_0 = 5 THz. Due to the shortened guided wavelength fulfilled by GPWG,[31,34] the device dimension is deeply subwavelength, offering new possibilities for rapid switching and modulation of nanoscale propagating plasmonic modes in the THz and infrared spectrum.

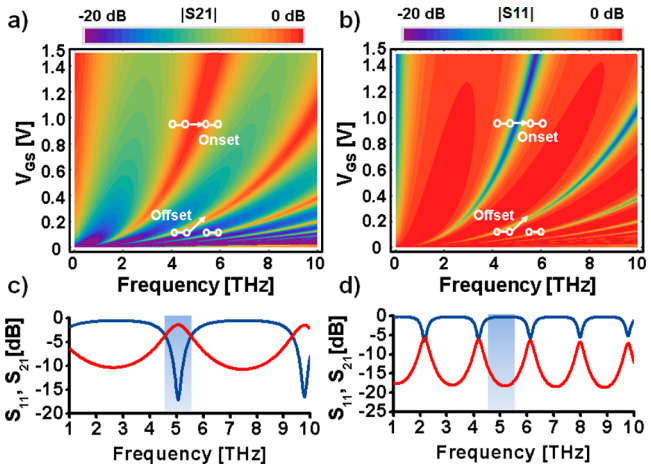

Figure 2. Contours of (a) transmission and (b) reflection of the graphene nanodevice in Figure 1c for V_{DS} = 0, varying the frequency and V_{GS}; (c) Transmission (red) and reflection (blue) spectra for V_{GS} = 1 V; (d) is similar to (c), but for V_{GS} = 0.12 V.

More interestingly, the integration of more than one gate may realize a number of THz nanodevices and nanocomponents, with reconfigurable and electronically programmable phase-shifting, filtering, coupling, and matching functionalities. Figure 1d, as a practical example in this direction, shows an integrally gated (multigate) graphene nanodevice and the corresponding TLM at V_{DS} = 0, which can be modeled as a multistage, tunable transmission-line. We first consider the design of a THz phase shifter for phased-array antennas and dynamic digital beamformers based on this concept. In this case, each gated segment is seen as a binary bit, which is properly biased to provide a phase shift $\Delta\phi_i = (\beta_{i,on} - \beta_{i,off})L_i$, where $\beta_{i,on}$ and $\beta_{i,off}$ are the phase constants of the ON-state and OFF-state, respectively. For an N-bit phase shifter with N integral gates, the total phase shift $\Delta\phi = \sum_{i=1}^{N}\Delta\phi_i$ is obtained. In order to minimize the multiple reflections and return loss, the gate length of each binary bit is designed to be half of the guided wavelength in the ON-state ($\beta_{i,on}L_i = \pi$), while in the OFF-state, the real-part impedance of a bit $Z_{i,off}$ is designed to be the same as that of the input/output ports (source/drain lines). Under these assumptions, in order to achieve the desired phase shift and the impedance matching for all binary states, the following requirements for the "i"-th section need to be fulfilled:

dx.doi.org/10.1021/ph500046r | ACS Photonics 2014, 1, 647−654

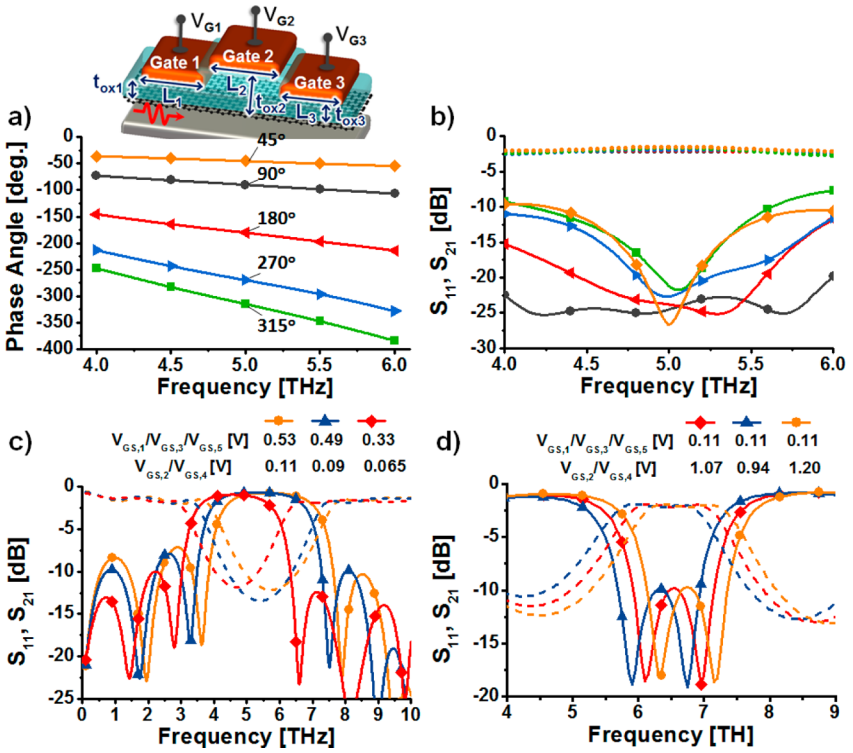

Figure 3. (a) Phase shift vs frequency for a 3-bit graphene-based phase shifter using three integrated gates. (b) Transmission (dashed) and reflection (solid) for the device in (a). (c) Transmission (dashed)/reflection (solid) vs frequency for a reconfigurable bandnotch filter constituted by the multigate graphene nanodevice in Figure 1d; (d) is similar to (c), but for a bandpass filter with modified gate length and biasing conditions.

$$\begin{cases} Z_{i,\mathrm{off}} = Z_S = Z_D \\ (\beta_{i,\mathrm{on}} - \beta_{i,\mathrm{off}})L_i = \Delta\phi_i \\ \beta_{i,\mathrm{on}}L_i = \pi \end{cases} \quad (2)$$

Figure 3a shows the numerical results for a 3-bit phase shifter consisting of three cascaded gated lines, which respectively provide phase shifts of 45° (bit 0), 90° (bit 1), and 180° (bit 2) at the operating frequency f_0 = 5 THz. By simply switching on and off of three binary bits, eight differential phase states $\Delta\phi$ = 0/45/90/135/225/270/315° can be obtained. As seen in Figure 3a, quite precise phase angles are obtained for different bias conditions. The optimum gate lengths and bias conditions can be obtained from (2). Here we choose the gate oxide thickness: $t_{ox,1} = t_{ox,3}$ = 22 nm, $t_{ox,2}$ = 25 nm, the gate length: L_1 = 190 nm, L_2 = 230 nm, L_3 = 305 nm, and the impedance of source/drain lines: $Z_S = Z_D = 60\eta_d d$. In the OFF-state, the bias voltage $V_{GS,1} = V_{GS,2} = V_{GS,3}$ = 0.11 V, yielding for the real-part impedance of the gated line the same value as the source/drain lines. The onset voltages of three binary bits are $V_{GS,1}$ = 0.18 V, $V_{GS,2}$ = 0.27 V, and $V_{GS,3}$ = 0.54 V, which respectively provide the desired phase differences of 45°, 90°, and 180° at the operating frequency. Figure 3b shows the transmission and reflection of this phase shifter, showing excellent input return loss and insertion loss at 5 THz. This graphene phase shifter may pave the way toward practical realization of THz beamforming, beamshaping, and spatial-multiplexing systems.

In addition to phasing THz signals within a short distance, the proposed integrated graphene nanodevice can also modulate the characteristic impedance of GPWG by varying V_{GS}; here we still assume V_{DS} = 0. One straightforward and practical application consists in realizing a THz low-pass filter (LPF) or "high-Z, low-Z filter"[39] realized within the same multigate graphene nanodevice in Figure 1d. When a large V_{GS} is applied to a gated short segment (which leads to a significant shift-up of Fermi level), its impedance can be much lower than the source/drain line, thereby being equivalent to a shunt capacitor. On the other hand, when a low V_{GS} is applied, a gated short segment may give a high impedance, being equivalent to a lumped inductor. A stepped-impedance LPF can therefore be realized by electronically programming multiple gated lines connected in series, with real-time tunability.

By properly modulating the phase and impedance, various filtering functions can be achieved at THz frequencies. In the following, we design bandpass and bandnotch filters using the proposed integrally gated graphene nanodevice comprising of five gates, as shown in Figure 1d. Here we assume a source/drain line impedance $Z_S = Z_D = 65\eta_d d$. For the bandnotch filter design, gates 1, 3, and 5 are biased with a high voltage, while gates 2 and 4 are biased with a lower voltage. We choose the gate lengths $L_1 = L_3 = L_5$ = 140 nm, $L_2 = L_4$ = 60 nm, and the gate oxide thicknesses $t_{ox,1} = t_{ox,3} = t_{ox,5}$ = 25 nm, $t_{ox,2} = t_{ox,4}$ = 22 nm. Similar to a direct-coupled resonator filter, which utilizes a quarter wavelength transmission line as the *J*-admittance inverter,[39] the bandstop effect can be obtained by cascading several coupled quarter-wavelength sections separated by reactive diaphragms. Figure 3c shows the numerical results for this band-notch filter with different bias voltages setups. The band-notch function is clearly obtained around the center frequency of 5 THz, at which the first, third, and fifth gated transmission line segments are approximated as quarter-wavelength sections ($\beta_1 L_1 = \beta_3 L_3 = \beta_5 L_5 \approx 90°$) separated by the short second and fourth gated sections with much higher impedance, behaving like the postwall sections in a cavity filter.[39] From Figure 3c, we specifically note that the notched band is tunable by varying the bias voltages. Figure 3d is similar

dx.doi.org/10.1021/ph500046r | ACS Photonics 2014, 1, 647−654

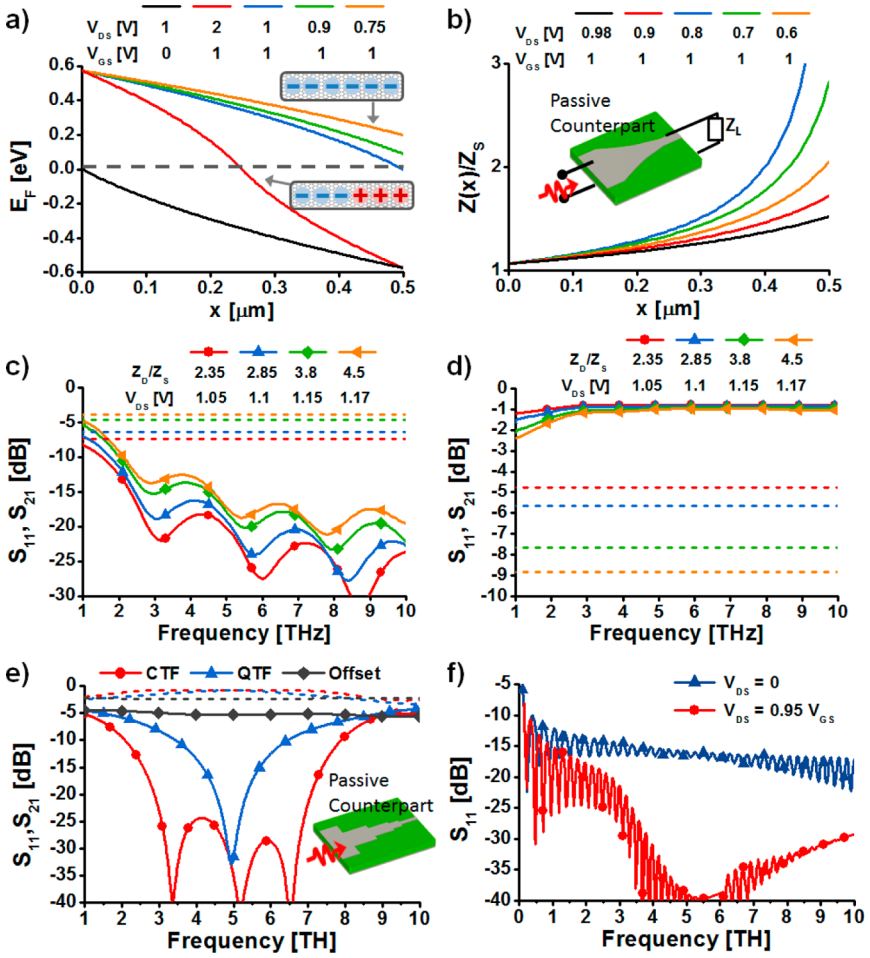

Figure 4. (a) Fermi energy and (b) characteristic impedance along the graphene waveguide channel (gated line) for the three-terminal (S−G−D) nanodevice in Figure 1c, with different biasing conditions. Here source and drain terminals are respectively located at x = 0 and 0.5 μm, and $Z_D > Z_S$. (b) Reflection and (c) transmission spectra for a graphene-based broadband transformer, adaptable for different values of Z_D/Z_S (solid); results without transformer (dashed) are also presented for comparison. (e) Reflection (solid) and transmission (dashed) spectra for a dual-bandwidth (Chebyshev - $\lambda/4$) transformer constituted by the integrally gated graphene nanodevice in Figure 1d. (f) Reflection spectra for a broadband THz terminator constituted by the graphene nanodevice in Figure 1c, with its drain open-circuited.

to Figure 3c, but for a bandpass filter. In this case, we use the same device structures, but change the gate lengths and the bias voltages. Here we choose the gate lengths $L_1 = L_3 = L_5 = 55$ nm and $L_2 = L_4 = 300$ nm. Gates 1, 3, and 5 are biased with low voltage, yielding high-impedance short segments, while gates 2 and 4, sandwiched by these high-impedance segments, are biased with a suitably high voltage to form half-wavelength resonators at the center frequency, thus, achieving the bandpass effect.[39] It is also seen in Figure 3d that the passband is also tunable by varying the bias voltages. The insertion loss of these graphene-based phase shifters and filters can be improved by using clean graphene with much higher carrier mobility and lower intraband scattering rate than the one considered here.

So far, the device operation has been limited to using a zero V_{DS}, while in the following we show that the three-terminal operation with nonzero V_{DS} and V_{GS} may realize even more complex operations, such as achieving spatially-variant, tapered impedance and phase profiles along the gated line, introducing new possibilities for designing broadband reconfigurable THz components. Considering the three-terminal graphene nanodevice in Figure 1c, Figure 4a, and Figure 4b, respectively, show the variations of E_F and characteristic impedance along a 0.5 μm long GPWG for such a device. When $|V_{GS}| > |V_{DS}|$, E_F decreases along the direction of signal propagation (x-axis), effectively producing a tapered transmission line, with impedance varying as a function of V_{GS} and V_{DS}. When $|V_{GS}| \leq |V_{DS}|$, the ambipolar field effect is obtained in GFET,[44−47] and therefore, E_F varies from positive (n-type channel) to negative (p-type channel).[48] Owing to the symmetry of the electronic band structure in graphene, both negative and positive signs of E_F provide the same complex surface conductivity.

One straightforward application of the proposed tapered transmission line is to make Klopfenstein-like impedance transformers used for matching arbitrary real load impedance over a wide bandwidth.[39] A Klopfenstein transformer is typically realized with multisection matching transformers, and in the limit of an infinite number of sections, it approaches a transmission line with continuously tapered impedance. Figure 4c and d, respectively, show the reflection and transmission spectra for a broadband THz transformer made of the graphene nanodevice in Figure 1c, which matches the source line ($Z_S = 25\eta_d d$) to the drain line with higher impedance (here $Z_D/Z_S > 2$) over a broad bandwidth provided that suitable V_{DS} and V_{GS} are applied. Here V_{GS} is fixed to 1.2 V, while V_{DS} is varied to match different load impedances at the

dx.doi.org/10.1021/ph500046r | ACS Photonics 2014, 1, 647−654

drain terminal. The reflection and transmission spectra without impedance transformer are also shown (dashed lines) for a fair comparison.

We stress that here we have used an approximate method[39] to calculate the reflection and transmission response of a continuously tapered transmission line, discretizing it into a number of incremental sections (i.e., 1000 sections here) with a small impedance change from one section to the next, as shown in Figure 1c. Then, signals reflected back to the source line (S_{11}) and passed to the drain line (S_{21}) can be calculated by the transfer matrix method. From Figure 4c,d, we observe broadband matching, effective for different values of Z_D/Z_S, thanks to the tunable and tapered impedance $Z(x)$ in the gate line. Instead of geometrically modifying the impedance like its passive RF counterpart in the inset of Figure 4b, different passband characteristics of this graphene-based transformer are achieved by changing the profile of tapered impedance via bias voltages V_{GS} and V_{DS}. We note that the multiple independent gated segments, as shown above, can also realize inhomogeneous impedance profiles, but with the major drawback of increased design and fabrication complexity, that is, the requirement of a large number of cascaded gates.

In order to make a comparison, we also propose a bandwidth-reconfigurable transformer[39,49] composed of a similar device with three integral gates. The impedance of source and drain lines are $Z_S = 22\ \eta_d d$ and $Z_D = 4\ Z_S$, respectively. For broadband Chebychev operation, $V_{DS} = 0$ and three gates are properly biased to achieve $\mathrm{Re}[Z_1]/Z_S = 1.2662$, $\mathrm{Re}[Z_2]/Z_S = 2$, and $\mathrm{Re}[Z_3]/Z_S = 3.1591$ at the center frequency $f_0 = 5$ THz. These optimal values are theoretically derived in ref 49. The physical length of each gate in the biased condition is designed to be one-quarter of the guided wavelength. For narrowband operation, the three gates are biased to achieve $\mathrm{Re}[Z_1] = Z_S$, $\mathrm{Re}[Z_3] = Z_D$, $Z_2 = (Z_D Z_S)^{1/2} = 2Z_S$, and $\beta_2 L_2 = \pi/2$, making a typical quarter-wavelength transformer with narrower bandwidth. Figure 4e shows the reflection and transmission spectra of this dual-bandwidth transformer, showing third-order Chebyshev-type broadband matching and first-order (λ/4-) narrowband matching, which are realized with the above biasing setups, tunable in real-time. It is noted that the matching bandwidth is narrower than the three-terminal operation in Figure 4c,d, while the fabrication complexity is increased.

The proposed three-terminal devices with tapered propagation properties can also be applied to various broadband applications, such as terminators and delay eqaulizers, to name a few. As an example, we design a broadband THz terminator (matched load), in which the open-circuit drain terminal ($Z_D \to \infty$) is biased with a DC voltage $V_{DS} = V_{GS} = 0.1$ V, resulting in exponentially tapered impedance. The low V_{GS} causes a low Fermi energy level and relatively high insertion loss in the graphene channel waveguide. We assume $Z_S = 69\eta_d d$ and a gate length $L_G = 2\ \mu$m, which is deeply subwavelength over the frequency band of interest (1−10 THz). Figure 4f reports the reflection coefficient versus frequency for this graphene terminator. It is noticed that when the device is biased as $V_{DS} = V_{GS} = 0.1$ V, reflections can be less than −20 dB over the entire bandwidth of interest. In contrast, if $V_{DS} = 0$, reflections are increased when operated without tapering the impedance in the gated line. This ultracompact and broadband terminator may be of interest for on-chip THz circuits, preventing signal interference and reverse gain.

Finally, in Figure 5a we envision a label-free, noninvasive THz biosensor, realized by the graphene nanodevice in Figure 2, combined with a nanofluidic delivery channel and lab-on-a-chip technology. The target molecules, cells, or tissues injected into the nanofluidic channel will flow through the gate line of the graphene nanodevice, being characterized and tagged by the transmission response of the THz signal. Since the electric field is strongly confined in the tunable GPWG, the transmission through the microcavity structure may sensibly depend on small perturbations of the refractive index of target biospecies $n_b$flowing through the gated region of graphene waveguide. We may adjust V_{GS} (here $V_{DS} = 0$ V), which in turn changes $\beta[n_b, E_F[V_{GS}]]$, to achieve Fabry−Perot-enhanced transmission at a monochromatic THz frequency of choice. As a result, biospecies can be tagged according to the measured S_{11}/S_{21} versus V_{GS} data. Here the design parameters are $L = 2\ \mu$m and $Z_S = Z_D = 3\eta_d d$. Figure 5b shows the transmission contours at the operating frequency of 5 THz, varying the index of the filling material and bias voltage. Figure 5d shows the detail S_{21} versus V_{GS} record, with $n_b = 1.4 \pm \Delta n_b$ and $\Delta n_b = 0.1$. The $S_{21} - V_{GS}$ signals may be able to identify the small refractive index variations caused by versatile intracellular bioevents. It is also known that many large proteins and DNA molecules have absorption due to collective vibrational and rotational modes in the THz and far-IR region,[50] which are considered as another bimolecular fingerprint. Due to the complex molecular structures of biomaterials, they may have different levels of absorption or electric loss tangent in the THz spectrum. Figure

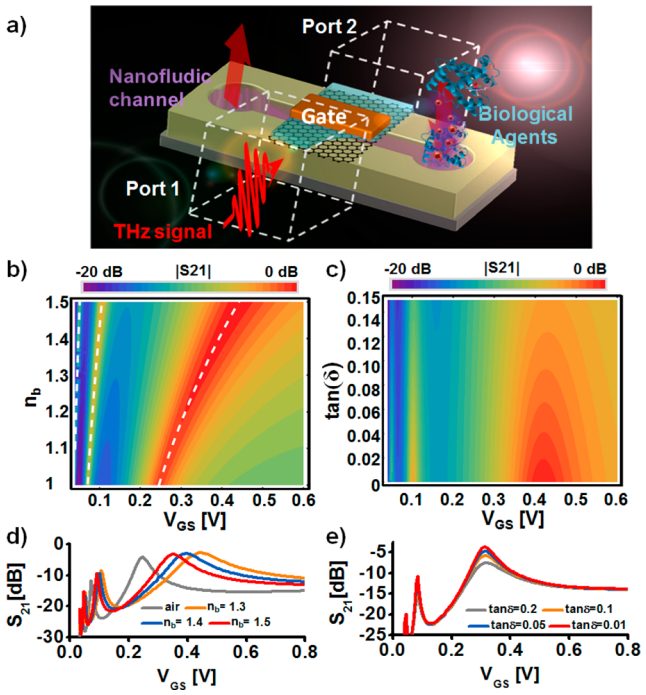

Figure 5. (a) Schematics of a THz biosensor composed of a nanofluidic delivery channel and the structure in Figure 1c; here $V_{DS} = 0$. (b) Contours of transmission for this graphene-based biosensor at 5 THz, varying V_{GS} and refractive index of material delivered through the channel; (c) is similar to (b), but investigating the influence of the material's loss ($\delta = \mathrm{Im}[\varepsilon]/\mathrm{Re}[\varepsilon]$). Transmission versus V_{GS} for materials with different values of (d) refractive index and (e) loss level at 5 THz, showing good sensitivity to changes in refractive index and absorption.

dx.doi.org/10.1021/ph500046r | ACS Photonics 2014, 1, 647−654

5c,e shows similar results varying the electric loss tangent of injected biospecies $\tan(\delta) = \mathrm{Im}[\varepsilon_b]/\mathrm{Re}[\varepsilon_b]$ (here $\mathrm{Re}[\varepsilon_b] = (n_b)^{1/2} = 2.1$). It is seen in Figure 5c,e that the magnitude of the transmitted signal is highly sensitive to different levels of loss. This graphene-based nanosensor may enable high-speed, coupler-free, and multifunctional lab-on-chip biosensors, being readily integrated within a THz monolithic integrated circuit to conduct real-time detection. Potential applications include genetic sequencing, drug and cancer screening, and forensic medicine.[50] In the Supporting Information we envision a nanofabrication route for the proposed hybrid electronic-plasmonic graphene nanodevices using semiconductor processes.

CONCLUSIONS

We have introduced a hybrid electronic-plasmonic graphene platform formed by a graphene plasmonic waveguide and a single/multiple-gate graphene transistor. we have shown that the proposed device architecture may be at the basis of a variety of integrated THz components, by simply tailoring the length and number of gates, as well as the bias voltages, realizing electronically programmable and fully reconfigurable integrated THz modulators, switches, phase-shifters, filters, matching networks, couplers, and attenuators for THz front-end circuits and systems. We envision that these graphene nanodevices may serve as the ideal physical layer for THz wireless communication, nanonetworks,[29] biosensing, nondestructive detection, and actuation due to their real-time reconfigurability and tunability, with exciting performance.

ASSOCIATED CONTENT

Supporting Information

Additional data. This material is available free of charge via the Internet at http://pubs.acs.org.

AUTHOR INFORMATION

Corresponding Authors

*E-mail: pychen@utexas.edu. Tel.: +1-512-826-5106; +1-313-577-3920.

*E-mail: alu@mail.utexas.edu. Tel.: +1-512-471-5922. Fax: +1-512-471-6598.

Notes

The authors declare no competing financial interest.

ACKNOWLEDGMENTS

This work was supported in part by the NSF CAREER Award No. ECCS-0953311, AFOSR with grant No. FA9550-13-1-0204, ARO with grant No. W911NF-11-1-0447 and Welch Foundation with grant No. F-1802, and the Norman Hackerman Advanced Research Program.

REFERENCES

(1) Novoselov, K. S.; Geim, A. K.; Morozor, S. V.; Jiang, D.; Zhang, Y.; Dubonos, S. V.; Grigorieva, I. V.; Firsov, A. A. Electric Field Effect in Atomically Thin Carbon Films. *Science* **2004**, *306*, 666−669.

(2) Geim, A. K.; Novoselov, K. S. The Rise of Graphene. *Nat. Mater.* **2007**, *6*, 183−191.

(3) Wong, H. S. P.; Akinwande, D. J. *Carbon Nanotube and Graphene Device Physics*; Cambridge University Press: Cambridge, 2011.

(4) Li, Z. Q.; Henriksen, E. A.; Jiang, Z.; Hao, Z.; Martin, M. C.; Kim, P.; Stormer, H. L.; Basov, D. N. Dirac Charge Dynamics in Graphene by Infrared Spectroscopy. *Nat. Phys.* **2008**, *4*, 532−535.

(5) Gusynin, V. P.; Sharapov, S. G.; Carbotte, J. P. Magneto-Optical Conductivity in Graphene. *J. Phys.: Cond. Matter* **2007**, *19*, 026222.

(6) Falkovsky, L. A.; Pershoguba, S. S. Optical Far-Infrared Properties of Graphene Monolayer and Multilayers. *Phys. Rev. B* **2007**, *76*, 153410.

(7) Hanson, G. W. Dyadic Green's Functions and Guided Surface Waves for a Surface Conductivity Model of Graphene. *J. Appl. Phys.* **2008**, *103*, 064302. Hanson, G. W. Dyadic Green's Functions for an Anisotropic, Non-Local Model of Biased Graphene. *IEEE Trans. Antenna Propagat.* **2008**, *56*, 747−757.

(8) Rana, F. Graphene Terahertz Plasmon Oscillators. *IEEE Trans. Nanotechnol.* **2008**, *7*, 91−99.

(9) Jablan, M.; Buljan, H.; Sojačić, M. Plasmonics in Graphene at Infrared Frequencies. *Phys. Rev. B* **2009**, *80*, 245435.

(10) Vakil, A.; Engheta, N. Transformation Optics Using Graphene. *Science* **2011**, *332*, 1291−1294.

(11) Chen, P. Y.; Alù, A. Atomically Thin Surface Cloak Using Graphene Monolayers. *ACS Nano* **2011**, *5*, 5855−5863.

(12) Chen, P. Y.; Soric, J.; Padooru, Y. R.; Bernety, H. M.; Yakovlev, A. B.; Alù, A. Nanostructured Graphene Metasurface for Tunable Terahertz Cloaking. *New J. Phys.* **2013**, *15*, 123029.

(13) Koppens, F. H. L.; Chang, D. E.; Garcia de Abajo, F. J. Graphene Plasmonics: A Platform for Strong Light-Matter Interactions. *Nano Lett.* **2011**, *11*, 3370−3377.

(14) Fang, F.; Wang, Y.; Schlather, A. E.; Liu, Z.; Ajayan, P. M.; García de Abajo, F. J.; Nordlander, P.; Zhu, X.; Halas, N. J. Active Tunable Absorption Enhancement with Graphene Nanodisk Arrays. *Nano Lett.* **2014**, *14*, 299−304.

(15) Bao, Q.; Zhang, H.; Wang, B.; Ni, Z.; Haley, C.; Lim, Y. X.; Wang, Y.; Tang, D. Y.; Loh, K. P. Broadband Graphene Polarizer. *Nat. Photonics* **2011**, *5*, 411−415.

(16) Ju, L.; Geng, B.; Horng, J.; Girit, C.; Martin, M.; Hao, Z.; Bechtel, H. A.; Liang, X.; Zettl, A.; Shen, Y. R.; Wang, F. Graphene Plasmonics for Tunable Terahertz Metamaterials. *Nat. Nanotechnol.* **2011**, *6*, 630−634.

(17) Chen, P. Y.; Alù, A. Terahertz Metamaterial Devices Based on Graphene Nanostructures. *IEEE Trans. Terahertz Sci. Technol.* **2013**, *3*, 748−756.

(18) Liu, M.; Yin, X.; Ulin-Avila, E.; Geng, B.; Zentgraf, T.; Ju, L.; Wang, F.; Zhang, X. A Graphene-Based Broadband Optical Modulator. *Nature* **2011**, *474*, 64−67.

(19) Liu, M.; Yin, X.; Zhang, X. Double-Layer Graphene Optical Modulator. *Nano Lett.* **2012**, *12*, 1482−1485.

(20) Fang, Z.; Thongrattanasiri, S.; Schlather, A.; Liu, Z.; Ma, L.; Wang, Y.; Ajayan, P. M.; Nordlander, P.; Halas, N. J.; García de Abajo, F. J. Gated Tunability and Hybridization of Localized Plasmons in Nanostructured Graphene. *ACS Nano* **2013**, *7*, 2388−2395.

(21) Yan, H.; Li, X.; Chandra, B.; Tulevski, G.; Wu, Y.; Freitag, M.; Zhu, W.; Avouris, P.; Xia, F. Tunable Infrared Plasmonic Devices Using Graphene/Insulator Stacks. *Nat. Nanotechnol.* **2012**, *7*, 330−334.

(22) Christensen, J.; Manjavacas, A.; Thongrattanasiri, S.; Loppens, F. H. L.; Garcia de Abajo, F. J. Graphene Plasmon Waveguiding and Hybridization in Individual and Paired Nanoribbons. *ACS Nano* **2012**, *6*, 431−440.

(23) Brar, V. W.; Jang, M. S.; Sherrott, M.; Lopez, J.J.; Atwater, H. A. Highly Confined Tunable Mid-Infrared Plasmonics in Graphene Nanoresonators. *Nano Lett.* **2013**, *13*, 2541−2547.

(24) Chen, J.; Badioli, M.; Alonso-Gonzalez, P.; Thongrattanasiri, S.; Huth, F.; Osmond, J.; Spasenovic, M.; Centeno, A.; Pesquera, A.; Godignon, P.; Elorza, A. Z.; Camara, N.; Garcia de Abajo, F. J.; Hillenbrand, R.; Koppens, F. H. L. Optical Nano-Imaging of Gate-Tunable Graphene Plasmons. *Nature* **2012**, *487*, 77−81.

(25) Lin, Y. M.; Valdes-Garcia, A.; Han, S. J.; Farmer, D. B.; Meric, I.; Sun, Y.; Wu, Y.; Dimitrakopoulos, C.; Grill, A.; Avouris, P.; Jenkins, K. A. Wafer-Scale Graphene Integrated Circuit. *Science* **2011**, *332*, 1294−1297.

(26) Ryzhii, V.; Ryzhii, M.; Mitin, V.; Shur, M. S.; Otsuji, T. Terahertz Photomixing Using Plasma Resonances in Double-Graphene Layer Structures. *J. Appl. Phys.* **2012**, *113*, 174506.
(27) Otsuji, T.; Wttanabe, T.; Boubanga Tombet, S. A.; Satou, A.; Knap, W. M.; Popov, V. V.; Ryzhii, M.; Ryzhii, V. Emission and Detection of Terahertz Radiation Using Two-Dimensional Electrons in III-V Semiconductors and Graphene. *IEEE Trans. Terahertz Sci. Technol.* **2012**, *3*, 63−72.
(28) Chen, P. Y.; Alù, A. A Terahertz Photomixer Based on Plasmonic Nanoantennas Coupled to a Graphene Emitter. *Nanotechnology* **2013**, *24*, 455202.
(29) Akyildiz, I. F.; Jornet, J. M. The Internet of Nano-Things. *IEEE Wireless Commun.* **2010**, *17*, 58−63.
(30) Tamagnone, M.; Gomez-Diaz, J. S.; Mosig, J. R.; Perruisseau-Carrier, J. Reconfigurable Terahertz Plasmonic Antenna Concept Using a Graphene Stack. *Appl. Phys. Lett.* **2012**, *101*, 214102.
(31) Chen, P. Y.; Argyropoulos, C.; Alù, A. Terahertz Antenna Phase Shifters Using Integrally-Gated Graphene Transmission-Lines. *IEEE Trans. Antenna Propagat.* **2012**, *61*, 1528−1537.
(32) Tonouchi, M. Cutting-Edge Terahertz Technology. *Nat. Photonics* **2007**, *1*, 97−105.
(33) Federici, J.; Moeller, L. Review of Terahertz and Subterahertz Wireless Communications. *J. Appl. Phys.* **2010**, *107*, 111101.
(34) Hanson, G. W. Quasi-Transverse Electromagnetic Modes Supported by a graphene Parallel-Plate Waveguide. *J. Appl. Phys.* **2008**, *104*, 084314.
(35) Wang, Y.; Hong, W.; Dong, Y.; Liu, B.; Tang, H. J.; Chen, J.; Yin, X.; Wu, K. Half Mode Substrate Integrated Waveguide (HMSIW) Bandpass Filter. *IEEE Microwave Wireless Compon. Lett.* **2007**, *17*, 265−267.
(36) Edwards, B.; Alù, A.; Young, M. E.; Silverinha, M.; Engheta, N. Experimental Verification of Epsilon-Near-Zero Metamaterial Coupling and Energy Squeezing Using a Microwave Waveguide. *Phys. Rev. Lett.* **2013**, *100*, 033903.
(37) Chen, P. Y.; Huang, H.; Akinwande, D.; Alù, A. Distributed Amplifiers Based on Spindt-Type Field Emission Nanotriodes. *IEEE Trans. Nanotechnol.* **2012**, *11*, 1201−1211.
(38) Veronis, G.; Fan, S. Bends and Splitters in Metal-Dielectric-Metal Subwavelength Plasmonic Waveguides. *Appl. Phys. Lett.* **2005**, *87*, 131102.
(39) Pozar, M. D. *Microwave Engineering*, 3rd ed.; John Wiley & Sons: New York, 2004.
(40) Gómez-Díaz, J. S.; Esquius-Morote, M.; Perruisseau-Carrier, J. Plane Wave Excitation-Detection of Non-Resonant Plasmons Along Finite-Width Graphene Strips. *Opt. Express* **2013**, *21*, 24856−24872. Correas-Serrano, D.; Gomez-Diaz, J. S.; Perruisseau-Carrier, J.; Alvarez-Melcon, A. Graphene Based Plasmonic Tunable Low Pass Filters in the THz Band. *arXiv:1304.6320*.
(41) Bolotin, K. I.; Sikes, K. J.; Jiang, Z.; Klima, M.; Fudenberg, G.; Hone, J.; Kim, P.; Stormer, H. L. Ultrahigh Electron Mobility in Suspended Graphene. *Solid State Commun.* **2008**, *146*, 351−355.
(42) Tao, L.; Lee, J.; Chou, H.; Holt, M.; Ruoff, R. S.; Akinwande, D. Synthesis of High Quality Monolayer Graphene at Reduced Temperature on Hydrogen-Enriched Evaporated Copper (111) Films. *ACS Nano* **2012**, *6*, 2319−2325.
(43) Tao, L.; Lee, J.; Li, H.; Piner, R. D.; Ruoff, R. S.; Akinwande, D. Inductively Heated Synthesized Graphene With Record Transistor Mobility on Oxidized Silicon Substrates at Room Temperature. *Appl. Phys. Lett.* **2013**, *103*, 183115.
(44) Parrish, K. N.; Akinwande, D. An Exactly Solvable Model for the Graphene Transistor in the Quantum Capacitance Limit. *Appl. Phys. Lett.* **2012**, *101*, 053501.
(45) Parrish, K. N.; Akinwande, D. Impact of Contact Resistance on the Transconductance and Linearity of Graphene Transistors. *Appl. Phys. Lett.* **2011**, *98*, 183505.
(46) Fang, T.; Konar, A.; Xing, H.; Jena, D. Carrier Statistics and Quantum Capacitance of Graphene Sheets and Ribbons. *Appl. Phys. Lett.* **2007**, *91*, 092109.
(47) Thiele, S. A.; Schaefer, J. A.; Schwierz, F. Modeling of Graphene Metal-Oxide-Semiconductor Field-Effect Transistors with Gapless Large-Area Graphene Channels. *J. Appl. Phys.* **2010**, *107*, 094505.
(48) Jo, I.; Hsu, I. K.; Lee, Y. J.; Sadeghi, M. M.; Kim, S.; Cronin, S.; Tutuc, E.; Banerjee, S. K.; Yao, Z.; Shi, L. Low-Frequency Acoustic Phonon Temperature Distribution in Electrically Biased Graphene. *Nano Lett.* **2011**, *11*, 85−90.
(49) Matthaei, G. L.; Young, L.; Jones, E. M. T. Microwave Filters, Impedance-Matching Networks, and Coupling Structures, Artech House Books: Dedham, MA, 1980.
(50) Menikh, A.; MacColl, R.; Mannella, C. A.; Zhang, X. C. Terahertz Biosensing Technology: Frontiers and Progress. *ChemPhysChem* **2002**, *3*, 655−658.